Journal of The
Electrochemical Society



# Sputtered Iridium Oxide Electrodes Optimization and Implementation for Impedimetric Identification of *S. aureus* and *P. aeruginosa* Biofilms

To cite this article: Francesco Grassi *et al* 2025 *J. Electrochem. Soc.* **172** 035501

*Journal of The Electrochemical Society*, 2025 **172** 035501

# Sputtered Iridium Oxide Electrodes Optimization and Implementation for Impedimetric Identification of *S.aureus* and *P.aeruginosa* Biofilms

**Francesco Grassi,[1,=] Charlotte Cums,[2,3,=] Dieter Cuypers,[1] Rik Verplancke,[1] Thijs Vackier,[2] David Schaubroeck,[1] Maxime Van Haeverbeke,[4] Hans Steenackers,[2] and Maaike Op de Beeck[1,z]**

[1]*Centre for Microsystems Technology (CMST), imec and Ghent University, 9052 Gent, Belgium*
[2]*Department of Microbial and Molecular Systems, Centre of Microbial and Plant Genetics (CMPG), KU Leuven, 3001 Leuven, Belgium*
[3]*Life Science Technologies Department, imec, 3001 Leuven, Belgium*
[4]*Department of Data Analysis and Mathematical Modelling, KERMIT Research Unit Ghent University, 9000 Gent, Belgium*

Electrochemical impedance spectroscopy (EIS) has been established as an effective technique for bacterial biofilm detection. Through the need for miniaturization, the application of novel electrode materials gains interest. In this study, we introduce Sputtered IRidium Oxide Film (SIROF) electrodes of varying sizes and geometries as sensors for biofilm detection. Pre-emptive cyclic voltammetry (pre-cycling) was used to transform as-sputtered anhydrous iridium oxide films into hydroxides, reducing the impedance and allowing the material to be adopted for miniaturized biofilm sensors. Our investigation showed that especially lower scan rates during this pre-cycling process reduced the interfacial impedance, hence optimizing electrode performance for this application. Using EIS in combination with pre-cycled SIROF electrodes, we detected biofilm growth within 24 hours and successfully distinguished between biofilms of *S. aureus* and *P. aeruginosa*. Additionally, we analyzed the influence of electrode size on biofilm detection and characterization. This study highlights SIROF electrodes as a promising platform for sensitive and scalable biofilm monitoring.

 [DOI: 10.1149/1945-7111/adbdf2]

Manuscript submitted November 30, 2024; revised manuscript received February 10, 2025. Published March 19, 2025. *This paper is part of the JES Focus Issue on Trends and Biohybrid Approaches in Microbial Electrochemical Systems.*

Supplementary material for this article is available online

***Bacterial biofilms and current detection pitfalls.***—Bacterial biofilms are complex, diverse communities of bacteria embedded in a self-produced extracellular matrix.[1] Biofilms form as heterogeneous 3D structures, attached to a surface, with varying compositions. They contain bacterial cells, proteins, lipids, lipoproteins, nucleic acids, and polysaccharides like cellulose.[2–4] These structures have different microenvironments, which vary in pH, oxygen concentration, and metabolic activity.[5] Their nature makes them more resistant to antibiotics, disinfectants and other stresses versus planktonic cells.[6] They cause widespread issues in different environments, leading to significant financial consequences.[7] Biofilms cause up to 80% of all infections in healthcare. They are a major factor in those infections associated with medical devices.[6,8–11] The bacteria that cause infections in humans most often are known as ESKAPE. This includes *Enterococcus faecium*, *Staphylococcus aureus*, *Klebsiella pneumoniae*, *Acinetobacter baumannii*, *Pseudomonas aeruginosa*, and *Enterobacter* species.[12] *S. aureus* is the most common cause of implant-related infections, followed by *P. aeruginosa*.[13]

As antibiotic resistance in pathogens is on the rise, identifying them before treatment is vital.[14] Rapid detection and characterization of such an infection is crucial, it enables effective intervention with the right antibiotic.[14] Biofilm related infections are difficult to diagnose, with laborious, invasive, and time-intensive sampling and culturing methods as current standard practices.[15] Bacteria from biofilms can have slower growth rates, which may cause false negatives if they are not detected after the usual 48 h growth window.[16–18] More advanced tests use molecular detection techniques, which destroy the original sample.[18] On top of these issues, the above-mentioned methods are not real-time and not biofilm-specific. Any novel detection method should be able to detect and distinguish between these species, as well as be safe for use in vivo. To conclude, there is a clear need for a fast, safe, easy, and affordable detection method that is reliable and miniaturiseable.

Several innovative techniques have been proposed recently. Hyper-spectral imaging can, for example, determine the microbial composition of a biofilm.[19] Chemical techniques such as MALDI-TOF mass spectrometry (MS) can be used to distinguish between biofilm and planktonic cells.[20] However, these methods require expensive and large equipment, training, calibration, can lack specificity, and cannot be applied in vivo.[11,15,21,22] Another example uses a heatable capacitive sensor structure (CSS) to detect biofilms via their dielectric properties, which can differentiate between inherent moisture (abiotic) and biofilm (biotic). They are, however, sensitive to noise and interferences.[23,24] Finally, acoustic sensors have been employed for biofilm detection in water pipes, providing real-time detection.[25] They can however only detect biofilms of a certain thickness and are affected by the surrounding material. Both of these last examples cannot be implemented in vivo due to the necessary heating and possible distortions of the signal. Here, we propose EIS as a valuable alternative.

***EIS sensing using iridium oxide electrodes.***—Electrochemical impedance spectroscopy (EIS), combined with dedicated electrodes, is a promising technique for in situ, real-time biofilm detection. EIS is widely used as it is a relatively simple electrical method (i.e. a sinusoidal perturbation to the system), it can be automated, and the obtained information is dense, allowing the extraction of charge transfer properties between electrodes and fluids. It is a safe method, with bioimpedance measurements commonly used to monitor body composition.[26] Biofilm detection using EIS has been demonstrated with various sensors, often featuring interdigitated gold electrodes, in static or dynamic setups,[27–31] and sometimes with sensitivity-enhancing polymer coatings like PEDOT-PSS.[32,33]

[=]Equal Contribution.
[z]E-mail: Maaike.OpdeBeeck@imec.be

Miniaturization of electrodes in microelectrode arrays further enhances detection by providing spatially resolved data that reveals biofilm heterogeneity and aids classification, which increases their potential for use in vivo.[34,35] However, the high interfacial impedance of gold electrodes at sub-millimeter scales inhibits their application for biofilm detection. Our previous work addressed this limitation by using Titanium Nitride (TiN) as an electrode material, due to its low interfacial impedance with respect to common alternatives such as platinum and gold.[36,37] While effective in biofilm detection, the TiN electrodes proved problematic during cleaning and disinfection due to their porous and columnar structure, hence TiN electrodes are unreliable for repeated use. To overcome this, we propose Iridium Oxide (IrOx) as an alternative. IrOx microelectrodes offer low interfacial impedance when used in fluids, fabrication compatibility with standard cleanroom processing, and can be cleaned well, making them suitable for repeated usage.

Iridium oxide is a commonly used electrode material in several fields. Iridium oxide films can be fabricated using various methods, resulting in different properties, tailored to specific applications.[38] For instance, IrOx is extensively employed in pH electrodes due to its redox sensitivity to $H^+$ concentration and its fast response.[39–43] Multiple publications have detailed the manufacturing, calibration, and application of iridium oxide pH sensors for use in biofilm research.[42–44] Dexter et al. for example successfully implemented them to determine pH profiles, detailing variations within natural marine biofilms.[45]

While pH sensors are simple and straightforward, they only provide information about the acidity/alkalinity of the biofilm environment. By measuring resistive and capacitive properties, EIS offers a more complete picture of the biofilm's electrochemical characteristics. This includes details on the electrode-biofilm interface, biofilm conductivity, and overall structure. Additionally, it provides information about the medium above the biofilm, containing cells and metabolites, which influence conductivity. Another existing application of IrOx electrodes is their use in neuronal implants like deep brain stimulation (DBS) hardware.[46] To further emphasize their potential for use in biofilm detection, an increase in impedance in DBS electrodes has been described as an early indicator of bacterial infection.[47]

In this work, a Sputtered IRidium Oxide Film (SIROF) was selected, being compatible with standard microfabrication. SIROF is chemically and mechanically stable in aggressive environments such as the human body and has a low interfacial impedance in saline solutions. SIROF is usually deposited as an amorphous and anhydrous film through reactive sputtering, and a wide variety of sputtering strategies have been proposed in literature. As an alternative, a porous Activated IRidium Oxide Film (AIROF) can be formed on top of metallic iridium upon potential cycling in saline solutions or aqueous acids.[48–50] Despite the differences between SIROF and iridium regarding the initial stoichiometry, potential cycling in physiological saline solutions has also been shown to be beneficial for SIROF layers, which can be morphed into oxy-hydroxides of non-compact nature.[51] The need for pre-emptive cyclic voltammetry to optimize electrode characteristics of anhydrous SIROFs has been widely addressed[51–59] and is especially crucial for the SIROF films used for biofilm detection, due to the need for a low electrode impedance. However, to the understanding of the authors, no systematic test has been performed to show the impact of the scan rate used during preemptive potential cycling (pre-cycling) on the final state of the electrodes. Therefore, in this paper, we investigate the impact of the scan rate on microelectrode impedance reduction.

Secondly, the biofilm detection possibilities of SIROF electrodes using EIS are investigated. Toward this end, we studied *S. aureus* and *P. aeruginosa* biofilms, two healthcare industry relevant bacterial species. We conceptualized an optimization process for the electrodes' preparation (pre-cycling), and have provided a tangible proof-of-concept for their application to detect and differentiate between these bacterial species' biofilms.

## Experimental

***SIROF sensor design and fabrication.—*** *Devices for biological experimentation.*—The fabrication of sensors for biofilm characterization was performed on 2-inch squared borosilicate glass substrates. To start, the substrates were patterned with AZ® nLOF2070 negative photoresist (Microchemicals), followed by DC-sputtering of 15 nm titanium/160 nm platinum, which was then selectively lifted-off to create pads and interconnections. Next, 300 nm $SiO_2$ was deposited using PECVD (Oxford Plasmalab® 80Plus), and openings were made at the pads and at the electrodes sites through reactive ion etching. Finally, 15 nm titanium/70 nm iridium oxide was DC-sputtered to form the electrodes, using the same lift-off process that was employed for platinum. Both platinum and SIROF were DC-sputtered with a Leybold Z550 sputtering system (Leybold GmbH, Germany). Argon was used as inert gas for both deposition steps, $O_2$ was used as reactive gas for SIROF. Further comments on the chemical composition of the SIROF layers can be found in the Supplementary material.

To gain insights into the impact of electrode design on biofilm detection, a wide variety of electrode sizes and shapes was used. On each sample, 12 microelectrodes with geometrical surface areas (GSA), being 12 000 $\mu m^2$ (GSA-5), 26 000 $\mu m^2$ (GSA-4), 45 000 $\mu m^2$ (GSA-3) and 260 000 $\mu m^2$ (GSA-2) were fabricated. For each GSA group, three electrode shapes are patterned: a square, a circle, and a rectangle with a 4:1 length-to-width ratio. Finally, two 1 $mm^2$ squared electrodes were also included in the design (GSA-1) to test macro-electrodes for biofilm detection. An overview of the biofilm sensor is shown in Fig. 1 and the corresponding GSA groups are summarized in Table I. Having rough estimates of the thin film resistivity of in-house platinum films (~200 n$\Omega$ m), platinum interconnects were sized so that their electrical resistance would be less than 7 % (1/15) of the expected electrolyte resistance for each electrode in PBS at room temperature.[60,61]

*Pre-cycling optimization devices.*—Although preliminary electrochemical considerations were already made with the samples dedicated to biofilm detection, a separate set of devices was appointed to streamline validation and identification of effective pre-cycling protocols. These pre-cycling test devices followed a different fabrication process, i.e. a simplified version of the process described in earlier work by the authors[62] adapted for planar devices (i.e. no encapsulated CMOS chip). Silicon oxide was replaced by the combination of RIE-patterned polyimide (PI2610 and PI2611 from HD microsystems) sealed by the addition of wet-etched ALD layers (combination of aluminum and hafnium oxide deposited with an

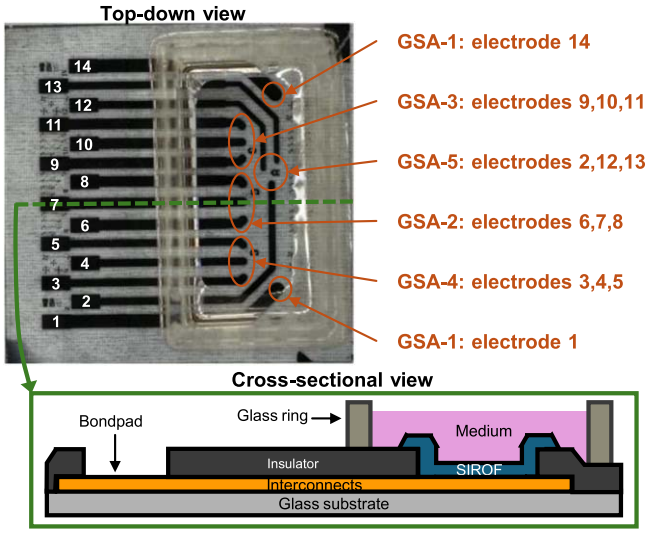


**Figure 1.** Biofilm sensor before usage for biofilm detection and schematic cross-section (not in scale).

Ultratech Savannah S200 G2 system). Plated gold was used for the interconnects. 15 nm titanium/70 nm platinum layer was sputtered just prior to SIROF deposition to replicate the same stack of materials as for the samples for bacterial testing. For this test device, 10 identical electrodes with geometrical surface areas (GSA) of 32 500 $\mu m^2$ and rounded rectangular shape were patterned. Since the SIROF fabrication was exactly the same for the biofilm sensors and the pre-cycling test devices, both devices exhibited nearly identical behavior.

***SIROF characterization and pre-cycling optimization.—*** *Electrochemical setup.*—After fabrication, all SIROF electrodes were immersed in unstirred, air-equilibrated Dulbecco's Phosphate Buffered Saline (D-PBS; Sigma-Aldrich, United States) for electrochemical pre-cycling and characterization of the electrodes. The electrolyte was at room temperature (between 19 and 23 °C). Both pre-cycling and characterization were performed with a commercial potentiostat (VSP model with a low-current option, BioLogic, France) connected to a 10-channel benchtop multiplexer (Keithley 7002 switching mainframe equipped with a Keithley 7158 low-current switching card) and in a 3-electrode configuration, using Ag/AgCl reference electrodes and a platinum grid as counter. Custom PCB adapters were produced to enable electrical connections between the devices with SIROF electrodes and the multiplexer inputs. All measurements were performed inside a Faraday cage.

*Pre-cycling optimization.*—Pre-emptive cyclic voltammetry is required to convert SIROF into a low-impedance oxy-hydroxide. This pre-cycling is also called activation. For all samples, a voltage window of -0.6 V to 0.8 V vs Ag/AgCl was selected based on pre-cycling protocols reported in literature.[51,52,54,55,59] Before and after pre-cycling, the impedance of each electrode was recorded at its open circuit voltage, using a 10 $mV_p$ sinusoidal as AC input voltage and [0.3; 100000]Hz as frequency measurement range.

For pre-cycling optimization devices, cyclic voltammetry at 7 different scan rates (0.01 V $s^{-1}$; 0.05 V $s^{-1}$; 0.25 V $s^{-1}$; 1 V $s^{-1}$; 5 V $s^{-1}$; 25 V $s^{-1}$; 100 V $s^{-1}$) was performed until a near-asymptotic behavior was reached. The assessment of near-asymptotic behavior is explained in the results Section of this paper. Under the stated conditions, the impedance recorded after pre-cycling is assumed to be the minimum attainable for a set scan rate value. To improve the test accuracy, the pre-cycling tests for each scan rates are performed 5 times, starting each time with pristine equally-sized electrodes. The significance of the differences among the impedance curves obtained for the 7 scan rates under test was assessed by performing a t-test on each available frequency value across all curve pairs.

***Biological experiments.—*** *Sample preparation for biological experiments.*—To prepare the devices for use, a custom rectangular glass well was adhered to the sensor surface to encompass all electrodes (see Fig. 1) using a biocompatible 2-component epoxy (Loctite® EA3430 epoxy adhesive; Henkel, Germany). The epoxy was cured at 60 °C for 1 h, after which the wells were washed thoroughly with demineralized water and dried. All electrode impedances were verified in Phosphate Buffered Saline (Gibco™ PBS, pH 7.4; Fisher Scientific, Belgium) using EIS measurements. Prior to use, the samples were conditioned using $UVO_3$ (15 min) (Jelight Company Inc.., United States) and sterilized using ethanol 70% (15 min). Sensors were then incubated overnight at room temperature with sterile Tryptic Soy Broth (TSB, Becton, Dickinson and Company, United States) growth medium to allow the baseline impedance to stabilize. All impedimetric responses were then again evaluated, which is used as a reference measurement. After this the samples were ready for bacterial inoculation.

*Bacterial cultures and biofilm formation.*—Overnight cultures (ON) of *Staphylococcus aureus* SH1000 and *Pseudomonas aeruginosa* PA14 were grown in Luria-Bertani (LB, VWR International, United States) broth (37 °C, shaking at 200 rpm). The optical density (OD; 595 nm) was adjusted to 0.32 ( $\approx 3.2 \times 10^8$cells $ml^{-1}$). ON cultures were centrifuged (3 min, 6000 rpm) and reconstituted in PBS twice. Next, the culture was diluted 1:100 in TSB. The sensor device wells were filled with 3000 µL of the diluted cell suspensions and statically incubated at 37 °C to allow biofilm formation. After 48 h of incubation, the medium was carefully removed and refreshed to provide new nutrients, allowing further biofilm growth over an additional 48 h. This experiment was performed in triplicate, using different ON cultures for inoculation in each repeat. After each experiment, the sensors were cleaned with a 1% solution of enzyme detergent (Tergazyme, Alconox USA) and incubating at 37 °C.

*Experimental EIS measurements of biofilms.*—An Ivium potentiostat (Ivium Technologies, the Netherlands) connected to a multiplexer (MUX) was used to sequentially measure all 14 electrodes on sensor devices. The IviumSoft app was used to measure the open circuit voltage and program the appropriate AC input voltage (20 $mV_p$) and 31 frequencies (ranging from 1 Hz to 100 kHz). Sensor devices were measured using custom connectors produced in-house (imec, Belgium) on a bench top at room temperature. An external large Pt electrode was used as a reference, with the counter shorted. Baseline measurements were taken of the sensor containing sterile TSB (Reference), directly after the addition of the bacterial cultures (T0) and subsequently after 24 , 48 , 72 and 96 h of incubation. At the 48 h time point, the impedance was measured before and after the medium renewal (referred to as '48 h Spent' and '48 h New'). Prior to each measurement, the sensors were removed from the incubator and placed at room temperature for 15 minutes to allow temperature stabilization.

*Data analysis.*—The EIS data was manually checked for outliers. The impedance magnitude $|Z|$, and the real and imaginary components were normalized versus the reference (sterile TSB) for each individual electrode $[(T_1 - T_0)/T_0]\cdot 100$ in order to remove any influence of sensor variability. The phase shift, $\Delta P$, was calculated by subtracting the phase at the reference measurement from other time points ($\Delta P = P_1 - P_0$). Data was grouped according to electrode size (see Table I and subsequently transformed using Principal Component Analysis (PCA), a statistical technique used to reduce the dimensionality of data while retaining most of its variability. PCA reduces the complexity of frequency-dependent impedance data, which helps distinguish between different bacterial biofilms based on their electrical impedance spectra. Median parameters were calculated and plotted using Python to evaluate spectrum changes over time. The median log transformed and normalized $|Z|$ change at 10 Hz and the median $\Delta P$ at 1.5 kHz over time were then portrayed using a heatmap, with annotated significances ($P<0.05$) as determined using a Wilcoxon signed rank test. Both frequencies are selected based on a clear indication in the EIS data of biofilm and medium effects, respectively. Lastly, maximal differences between both bacterial impedance spectra were determined within a lower frequency range for $|Z|$ and a higher frequency range for $\Delta P$. Significant differences were determined using a Mann-Witney U test and again annotated using asterisks on a heatmap.

**Table I. Electrode grouping by geometrical surface area.**

| Group | Electrodes | Total area, $\mu m^2$ |
|---|---|---|
| GSA 1 | 1,14 | $1.0 \times 10^6$ |
| GSA 2 | 6,7,8 | $260 \times 10^3$ |
| GSA 3 | 9,10,11 | $45 \times 10^3$ |
| GSA 4 | 3,4,5 | $26 \times 10^3$ |
| GSA 5 | 2,12,13 | $12 \times 10^3$ |

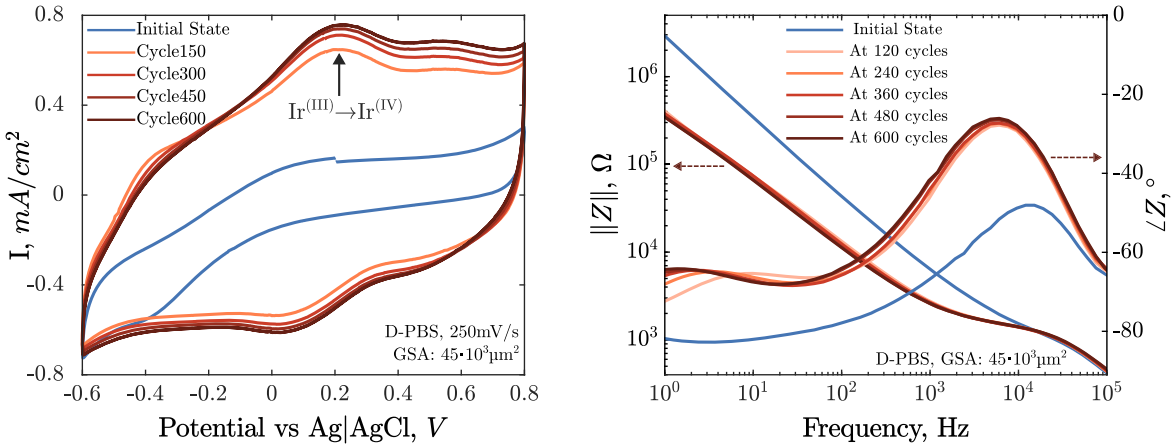


**Figure 2.** (a) Changes in CV response of a 70 nm-thick SIROF upon potential cycling between −0.6 V and 0.8 V vs. Ag|AgCl. (b) Changes in electrode impedance after potential cycling while approaching a steady state.

## Results and Discussion

***SIROF pre-cycling and cyclic voltammetry.***—Prior to usage, the as-sputtered SIROF electrodes required repeated potential cycling while being immersed in PBS. Typical changes in voltammograms during pre-cycling are shown in Fig. 2a. The voltammograms show a prominent anodic current peak at 0.2 V versus Ag|AgCl, related to the $Ir^{III} \rightarrow Ir^{IV}$ redox reaction as is previously reported for both AIROF and SIROF,[48,63] highlighting a continuous exchange of protons or hydroxide ions with the electrolyte, tentatively attributed to the redox reaction in Eq. 1.[64]

$$IrO_x(OH)_{n-x} + xH^+ + xe^- \leftrightarrow Ir(OH)_n \quad [1]$$

However, the current peak at 0.2 V is hardly visible in the initial voltammograms. This is related to the film composition directly after sputtering and is further discussed in the Supplementary material. Furthermore, the redox current peaks and the Charge Storage Capacity (CSC), i.e. the integral of the absolute current for each cycle, increase upon pre-cycling, which is likely evidence of progressive hydration of the SIROF films. As clearly seen in Fig. 2, the curent peaks and the CSC grow in a monotonic manner in subsequent voltammograms until a final -asymptotic- shape is reached.

In theory, the pre-cycling treatment is finished when this asymptote is obtained, although it might often result in an unnecessary long duration of the pre-cycling. Wessling et al.[51] reported that they morphed a full SIROF layer (350 nm thick, RF-sputter protocol with virtually zero metallic iridium) into an hydroxide by using a slow pre-cycling protocol (voltage sweep at 50 mV $s^{-1}$, using a window of -1.1 V to 1.3 V versus Ag|AgCl). The morphology changes across the whole SIROF thickness, but Wessling needed a pre-cycling of ∼53 h, which is long and thus impractical. Full conversion of the SIROF film was not achieved with excessively brief protocols. Using faster voltage scan rate might be an easy way to speed up the pre-cycling, although we were wondering whether a faster scan speed would also influence the depth of the SIROF being converted into an hydroxide, and whether it would influence the reduction of the interfacial impedance which is obtained after complete pre-cycling. In literature, we found reports about scan rates in the 0.05V $s^{-1}$ to 2.8 V $s^{-1}$ range for SIROF potential cycling prior to usage.[51–59] We decided to investigate a wider window: scan rates ranging from 0.01V $s^{-1}$ to 100V $s^{-1}$ are studied in this paper.

Before discussing how various pre-cycling scan affect the final electrode impedance, we will first explain how we determine the end point of a pre-cycling treatment. We chose to monitor the evolution of the $Ir^{III} \rightarrow Ir^{IV}$ anodic current peak, as detailed in the Supplementary material. Consequently, the magnitude of the anodic current peak was determined during the total pre-cycling treatment. To avoid the influence of some experimental inaccuracies, a fit of the current peak values was determined using a shifted 4-point logistic function. The current peak values for the first 75 cycles were always excluded to avoid instabilities. As the slope of the fitted function decreases as the SIROF comes closer to its final converted state, the derivatives of the fitted function are calculated and used for end point detection. Since all derivatives of the fitted current peaks with respect to cycle number rapidly decreased to values in the same order of magnitude while progressing toward an asymptotic state, a unique threshold of $3 \times 10^{-5}$ mA $cm^{-2}$ was visually determined and set as a strict end-point criterion for pre-cycling. An example illustrating the use of the described end point criterion is shown in Fig. 3b. Here, a derivative value of $3 \times 10^{-5}$ mA $cm^{-2}$ corresponds to a peak current value that is just 2 % lower than the value observed 2 h after the criterion was met. The decision of excluding the first cycles from the fit doesn't constitute a major limitation, since a near-asymptotic state is never reached so early.

Additionally, the shape of the voltammograms is clearly influenced by both the SIROF thickness and the as-sputtered stoichiometry, which is strongly related to the sputter conditions.[40] Different conditions may result in SIROF films containing different relative amounts of $Ir^{x+}$ species (x>0), some films include appreciable quantities of metallic iridium ($Ir^0$) after sputtering[65] and others show negligible amounts.[51] Hence, the protocol used to determine the end point of the pre-cycling treatment might differ if other sputter processes are used, since this will result in other shapes of the voltammograms.

***SIROF impedance.***—To gain a deeper insight in the relation between obtained SIROF impedance and pre-cycling, the impedance of electrodes in PBS is studied during cycling. For about 20 electrodes the impedance was determined every 120 cycles of the total pre-cycling process (scan rate 250 mV $s^{-1}$, as shown in Fig. 2b for a 46 000 µm² electrode. As expected, the impedance magnitude dropped during the pre-cycling in PBS for all electrodes. Interestingly, the decrease in impedance happens fast and only small remaining improvements are made in the final stage of the pre-cycling process. Further comments on why the impedance itself was not used as end point for pre-cycling are given in the Supplementary material.

***SIROF pre-cycling optimization.***—In this work, the direct impact of pre-cycling scan rate on electrode impedance was assessed by recording the impedance of equally sized-electrodes after extensive cyclic voltammetry at scan rates ranging from 0.01V $s^{-1}$ to 100V $s^{-1}$. Impedance changes due to pre-cycling at different scan rates are shown in Fig. 4. Positive t-test results reveal a significant

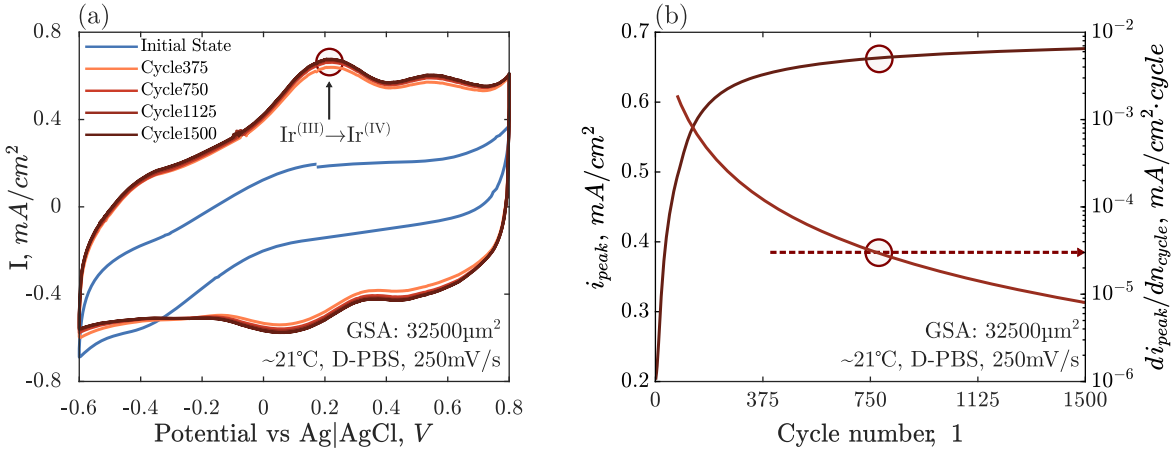


**Figure 3.** (a) Changes in CV response of SIROF after 1500 cycles at 250 mV $s^{-1}$ between -0.6 V and 0.8 V versus Ag/AgCl. (b) Change in anodic current peak during cyclic voltammetry at 250 mV $s^{-1}$. The circle indicates how at about 800 cycles (i.e. 2.5 h) the end point criterion for pre-cycling is met.

difference among all impedance magnitude curves, with the exception of 25V $s^{-1}$ versus 5V $s^{-1}$, as seen in Fig. 4.

A general remark on the impedimetric behavior of IrOx electrodes is warranted before delving into the impedance results for various scan rates. The typical decrease in impedance observed upon pre-cycling of iridium oxide electrodes is clearly in contrast with the behavior of standard metal electrodes in saline solution, since typical metal electrodes exhibit a constant capacitive behavior at low frequencies, commonly represented by a double-layer capacitance of approximately 20µF $cm^{-2}$.[66] IrOx electrodes are known to exhibit a pseudocapacitive behavior,[67,68] which means that typical IrOx reactions (such as Eq. in 1), despite being faradaic in origin, are highly reversible and hence artificially increase the equivalent capacitance at the electrode interface. This type of capacitive behavior is dependent on the electrode material as well as the electrolyte, as it is related to charge exchange at the interface between fluid and electrode. It is therefore addressed as "interfacial impedance". At very high frequency, this interfacial impedance becomes negligible and the main contribution to the electrode impedance is given by the electrolyte resistance, which is purely dependent on the electrolyte composition and electrode geometry.[60,61] Further details on the interfacial impedance can be found in the Supplementary material, where equivalent circuit modeling of the IrOx electrodes is described.

When looking at the impedance results for various scan rates in Fig. 4, we see that the impedance at the highest frequencies is very similar for the different scan rates. This is logical, since the impedance at high frequencies is mostly dependent on the electrolyte resistance, which is purely affected by the state of the electrolyte and is independent of the pre-cycling conditions. The small variability for each group which exists between the various scan rates can be attributed to the influence of the varying temperature and PBS evaporation on electrolyte resistivity at the time of each measurement.

For lower frequencies, the influence of the scan rate on impedance is very obvious: a lower scan rate is beneficial regarding the final obtained reduction in interfacial impedance. As the improvement in electrode impedance with pre-cycling is linked to hydroxide conversion,[51] the dependence of impedance on scan rate seen in Fig. 4 suggests that conversion of the SIROF film into a hydroxide is only taking place in the top part of the SIROF film and the thickness of this top part is increasing with lower scan rate. A possible explanation for the reported behavior is that density, morphology, and/or stoichiometry of the as-deposited layer hinders ion transport through the SIROF film at higher scan rates, just because there is insufficient time during 1 scan cycle for ions to reach the bottom on the SIROF film and cause hydroxide conversion. Because of the lower scan rate, also deeper located iridium in the film can be converted to its hydroxide state.

Based on the end point criterion that we previously discussed, the estimated duration of the pre-cycling process for each scan rate is determined and plotted in Fig. 5. It should be noted that for the lowest scan rate value, i.e. 10 mV $s^{-1}$, the end point criterion was not met after 3 days of pre-cycling, therefore an extrapolation was required. Even though the lower scan rates achieve greater reductions in interfacial impedance (as seen in Fig. 4), the total duration of

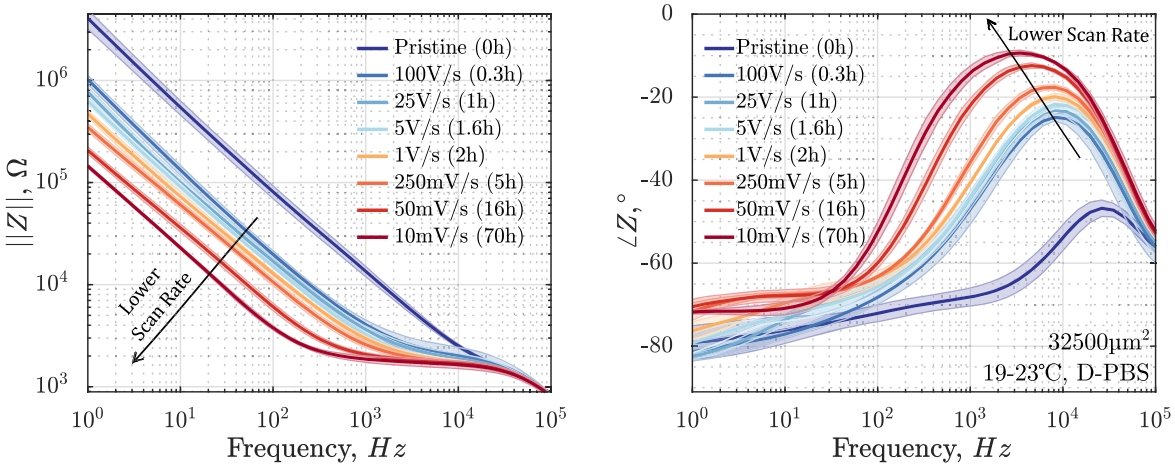


**Figure 4.** Impedance changes due to potential cycling in PBS between -0.6 V and 0.8 V versus Ag/AgCl using scan rates in the 0.01V $s^{-1}$ to 100V $s^{-1}$ range.

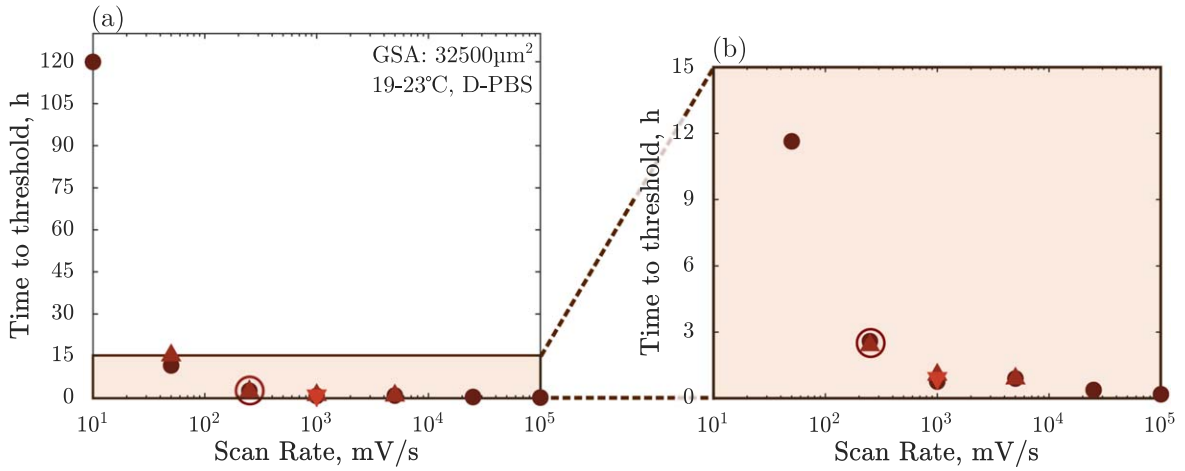


**Figure 5.** (a) Time to reach steady state of the anodic current peak during cyclic voltammetry of SIROF (value at 10 mV $s^{-1}$ scan rate is extrapolated). (b) Magnified Section from (a). 250 mV $s^{-1}$ is selected as a practical compromise.

pre-cycling needed with lower scan rates becomes excessively long (Fig. 5). For practical applications, a balance can be achieved by either pre-cycling at a moderate scan rate until the end point is reached or using the lowest scan rate with a more relaxed end point threshold to shorten the process. While neither approach achieves the maximum impedance reduction, both provide substantial improvements.

Such a compromise was made for the sensor devices applied to study the bacterial biofilms. The 250 mV $s^{-1}$ protocol was deemed to yield an acceptable impedance. As the impedance was showing limited changes before the end point criterion was met (see Fig. 2b), the duration of the protocol was further shortened from 800 cycles to 600 cycles, resulting in 2 h of continuous potential cycling for each electrode.

In theory, another alternative exists to reach very low electrode impedance after a shorter cycling duration: starting with less anhydrous as-sputtered films, hence films which are closer to a desirable electrochemical state will result in a shorter cycling duration. This can be realized by the use of dual-reactive sputtering with $H_2O$ or $H_2$ as additional feed gases.[55,69–73] However, water vapor in sputter tools is commonly regarded as a source of process variability, and its presence is therefore minimized in most sputter tools.[74] Moreover, proper handling of $H_2$ feed gases requires far greater safety measures if compared to $O_2$, especially for high-throughput sputtering systems, making $H_2$ less common as a feed gas.

***Sensor implementation.***— *Sensor performance.*—The implementation of the sensor for biofilm detection started by its preparation, as described in materials and methods, hereafter referred to as 'ring gluing'. Although electrode impedance was always recorded after pre-cycling, the stability over time of electrode impedance was deemed a possible concern. Before performing impedance measurements with biofilms, additional sanity checks in PBS were performed, as described in the 'Sensor implementation' section of the Supplementary material.

Additionally, we investigated the influence of electrode cleaning after biofilm detection. This is especially important in in vivo or in situ applications, where a sensor with an easily fouled or difficult to clean electrode could make biofilm removal through antibiotic treatment even more challenging. In Fig. 6, the typical impedance in PBS and TSB is shown before first usage as biofilm sensor, and after usage and cleaning. The minor variations in impedance measurements prove the reuseability of our SIROF electrodes. It is also clear that the impedance drastically changes after biofilm maturation on top of the electrodes, which will be discussed further in the next section.

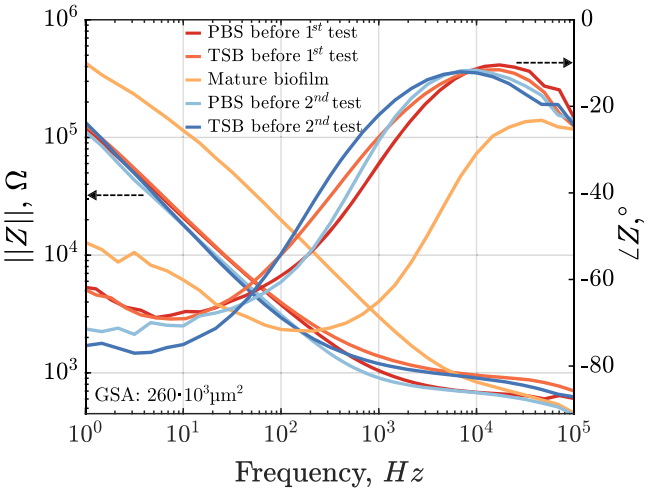


**Figure 6.** Typical changes in impedance upon usage for *P. aeruginosa* biofilm detection. Reference impedance in PBS and TSB shown on first usage and after ethanol cleaning.

*Bacterial biofilm characterization over time.*—We used *S. aureus* and *P. aeruginosa* as model organisms for biofilms formed in the medical field. To recap, the sensor well was filled with TSB after which the baseline impedance was measured (Reference). After this, the diluted cell suspensions in TSB were added. As the bacteria attach to the surface, proliferate and produce matrix, the impedance spectrum changes. After 48 h of incubation, the medium was carefully replaced. EIS measurements were performed directly after inoculation (T0), after 24 h and 48 h of incubation, a second time at 48 h but directly after medium replacement (called '48 h New'), and further after 72 h and 96 h of incubation. The normalized impedance plots for both bacteria over all time points are shown in Fig. 7 for the GSA 2 electrode subset.

Clear changes in normalized $|Z|$ (Figs. 7a and 7c) and $\Delta p$ (Figs. 7b and 7d) were observed with increasing incubation time for both bacteria. As biofilms are complex and irregular structures, a non-negligible standard deviation (shown as shaded area around each line) was found for each time point. Interestingly, the inoculation (T0) affects the impedance, showing notable variability that differs from subsequent trends. We observe a $|Z|$ increase in lower frequencies (LF, between 1 and 100 Hz), and a decrease at higher frequencies (HF, around $1 \times 10^4$ Hz).

As has been described previously in numerous publications, the increase in $|Z|$ LF can be attributed to biofilm growth.[32,33,75–88] As

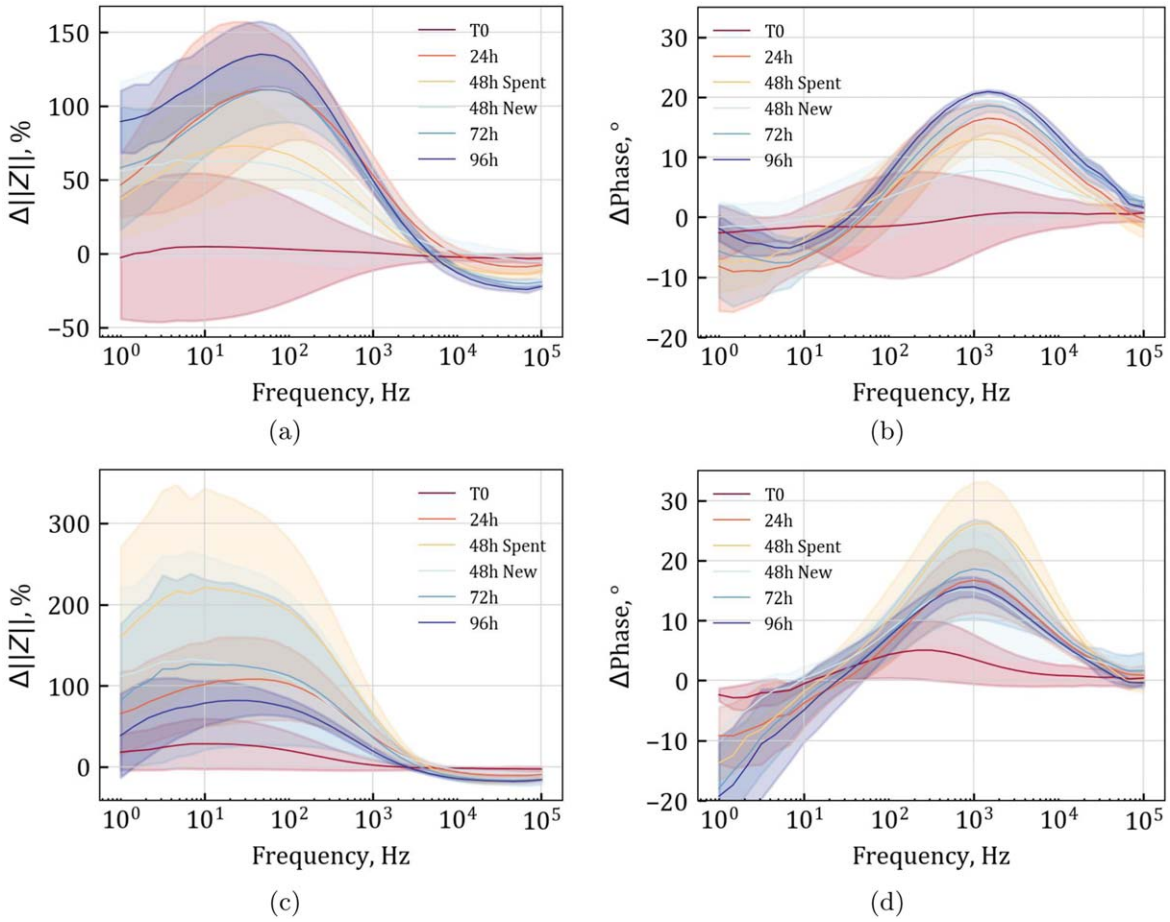


**Figure 7.** Normalized impedance over time for *P. aeruginosa* $\Delta|Z|$ (a) and $\Delta$P (b) and *S. aureus* $\Delta|Z|$ (c) and $\Delta$P (d) for GSA 2 electrodes.

bacteria attach to the surface, proliferate, and produce matrix compounds, the biofilm grows into a larger 3D structure. This structure influences the electrochemical properties at the electrode surface, affecting the impedance at LF. The increase in interfacial impedance is believed to be caused by the full coverage of the electrode surface by the mature biofilm. As a consequence, the active area of the electrodes available for charge exchange with the electrolyte is diminished. A mature biofilm can act as a physical barrier between electrode and electrolyte, effectively blocking the current.[34]

The impedimetric responses of the electrodes after biofilm growth were modelled using the ECM as described in the Supplementary material. We compare the parameters extracted in PBS and sterile TSB with those obtained after biofilm formation. The elements observed at lower frequencies were modeled as $CPE_{dl}$ (electrostatic double layer capacitor), $C_{\phi}$ (capacitance related to IrOx-specific faradaic-reaction-like processes) and $R_{ct}$ (faradaic resistance to charge transfer). Only $CPE_{dl}$ parameters Q and $\alpha$ show a clear trend during biofilm growth (Fig. S7). Q decreases during biofilm growth for both bacteria, whereas $\alpha$ decreases for *P. aeruginosa*, but has a more variable change for *S. aureus*. Both parameters shift closer to reference values at 48 h New for *P. aeruginosa*, which is not seen in the *S. aureus* data. A more in depth description of the changing parameters can be found in Supplementary material.

Impedance changes in the higher frequencies have long been described as arising from the resistance of the bulk solution ($R_{sol}$).[29,30,34,35,75,76,81,86,87,89–106] The decrease in impedance at HF can be interpreted as bacteria metabolizing low-conductivity substrates into smaller, highly charged molecules. This causes an increase of ionic strength in the medium, and thus a decrease in $R_{sol}$ (see Fig. S8).[75,107] It is important to note that the ionic composition of the medium within a distance similar to the electrode size is crucial, as it largely determines measured electrolyte resistance.[60,61]

To quantify the change in impedance over time, the log transformed and normalized $|Z|$ medians at LF (10 Hz) (see Figs. 8a and 8b) and the $\Delta$P medians at HF($1.4 \times 10^3$ Hz) (see Figs. 8d and 8e) were visualized using a heatmap (with * indicating $P<0.05$). Both bacteria show a significant difference in impedance after 24 h in $\Delta|Z|$ and $\Delta$P. The medium renewal at '48 h New' lowers the impedance, effectively removing any significant change previously measured for *P. aeruginosa*. For *S. aureus*, the measurement at 48 h with renewed medium still results in a significant change.

We observe an influence of the electrode sizes on their sensitivity to changes caused by biofilm growth when considering GSA 1 and 2 (largest electrodes), which exhibit larger differences earlier on and throughout in $\Delta|Z|$. Even though GSA 5 (smallest electrode) seems to not be able to confidently capture surface-related impedance changes, it does measure differences in the medium ($\Delta$P). Generally, significant changes over time are more clearly observed in $\Delta$P. GSA 3 and 4 show significant changes for *P. aeruginosa*, but fall short at later time points for *S. aureus*. Here, it is possible that this change is caused by a detachment of the biofilm in that area.

*Bacterial biofilm differentiation.*—To determine whether the SIROF electrodes can distinguish between both species, we investigated the difference in $\Delta|Z|$ at LF and $\Delta$P at HF between the bacteria, for each electrode group over time (see Figs. 8c and 8f respectively). Differences between the bacteria are significant after 24 hours in $|Z|$ LF as well as $\Delta$P HF. Interestingly, even the smallest

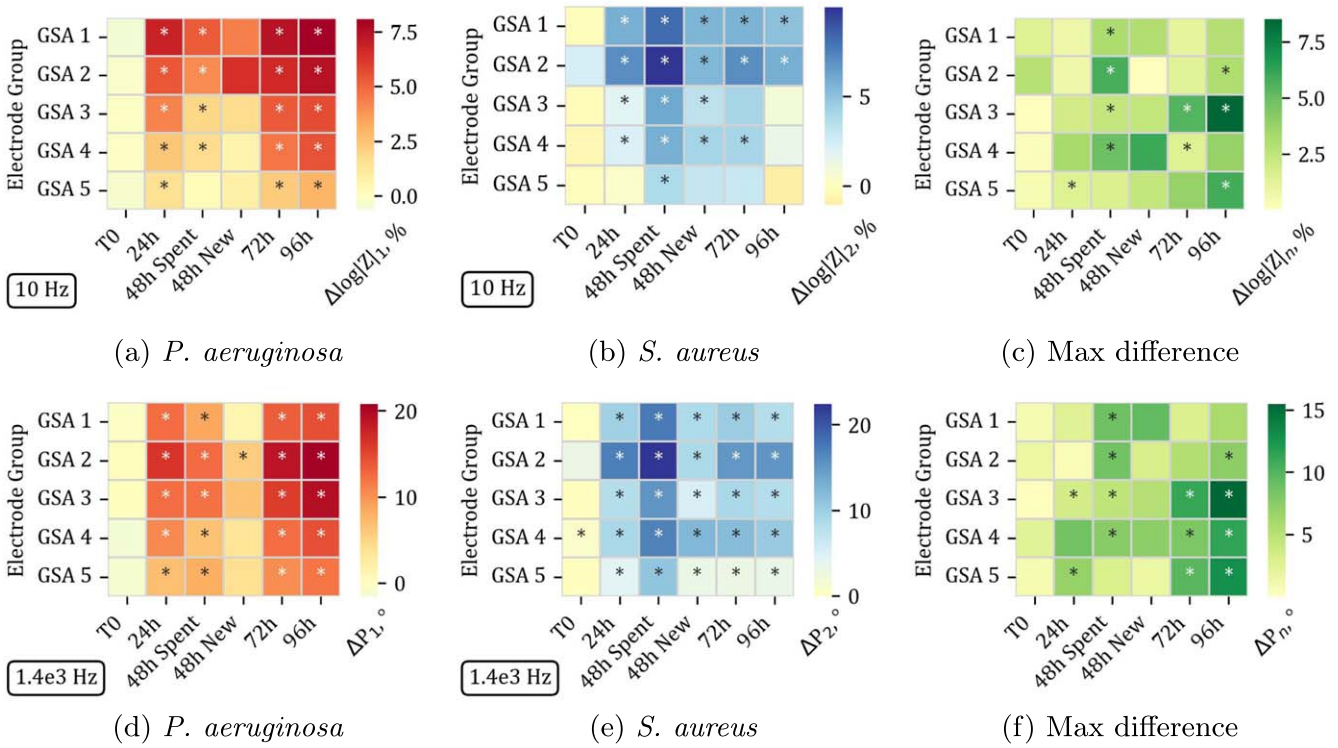


**Figure 8.** Median impedance for electrode groups over time for *P. aeruginosa* (reds) and *S. aureus* (blues), with normalized $\Delta log|Z|$ at 10 Hz (a and b) and $\Delta$P (d) at $1.4 \times 10^3$ Hz for (d and e). Maximal difference in impedance between bacteria ($\Delta_n = \Delta_1 - \Delta_2$) (greens), showing normalized $\Delta log\,|Z|_n$ (c) and $\Delta P_n$ (f).

electrode size (GSA 5) is able to capture the difference at LF as well as HF. No differences were observed between bacteria at '48 h New', this time point also failed to capture a difference versus the reference in *P. aeruginosa*.

There are some notable differences between these bacteria that could influence this disparity. *P. aeruginosa* produces pyocyanin, a redox-active phenazine, which influences the biofilms architecture and has been described to have a distinct electrochemical signature.[27,108] Pyocyanin facilitates electron transfer between the electrode and bacterial cells, which increases the overall conductivity at the biofilm-electrode interface. Ward et al. identified this metabolite in the supernatant above *P. aeruginosa* biofilms, and reported a specific reduction in impedance within the 10 -100 Hz range.[108] Interestingly, we observe changes in the same frequency range. Additionally, Ward et al. found a much smaller reduction in impedance for a mutant *P. aeruginosa* strain unable to produce pyocyanin, indicating its significant contribution to $\Delta|Z|$.

*P. aeruginosa* biofilms often display a mushroom-like, structured architecture with voids and channels for nutrient flow,[109] with a hydrophilic and negatively charged matrix.[110] It is possible that the renewal of the medium at 48 h, even though executed carefully, removes a large part of the mushroom-like biofilm structure of *P. aeruginosa*, therefore causing a decrease in impedance and shift closer to reference values. *S. aureus* biofilms are usually more densely packed and less structured. Here, the medium change could affect the biofilm less, thus causing less of a change in impedance. The largest differences between both biofilms (from $|Z|$ LF) were found at 48 h, 72 h and 96 h for GSA 3. While GSA 1 and 2 (larger electrodes) may be more sensitive to changes in impedance over time, it is possible that they fail to capture differences in biofilm microenvironment necessary for classification at later time points.

There has been extensive research on *P. aeruginosa* detection, specifically though these above-mentioned metabolites, implementing various methods.[111–118] Our proposed technology has a broader application, which is important for its potential to be implemented outside of the lab environment. These two species selected as model organisms are vastly different in their phenotype. If different species or even subspecies that are more similar to each other are selected to be grown on these electrodes, this classification will become more and more difficult. Further experiments considering additional healthcare relevant species and subspecies could determine if the electrodes are sensitive enough to capture smaller differences or identify specific pathogens in a multispecies biofilms. As previously demonstrated by Van Haeverbeke et al.,[35] there is potential in the use of predictive decision tree ensemble classifiers for bacterial classification up to a subspecies level.[35] Feeding impedimetric data of biofilms on the SIROF electrodes into such a predictive model could, after extensive model training, therefore facilitate their identification. Additionally, as demonstrated by Sheybani et al., there is benefit of combining multiple sensing methods for an increased accuracy.[80] Their implementation of a combined EIS and pH sensor for the detection of wound bacteria is especially interesting, since IrOx is a material frequently used in pH sensors.

*PCA of biofilm EIS data.*—To gain a more in depth understanding of the overall influence of the biofilm growth on the impedance and to capture trends in the dataset, we performed a PCA. This encompasses the full frequency spectrum of log transformed and normalized $|Z|$, Zim, Zre and Phase over time (See Fig. 9). The data points in the scatter plot represent data for *P. aeruginosa* in red and *S. aureus* in blue, in a range of hues to portray time points and differentiated by marker style for each electrode group. The first principal component (PC1) explains 88.82% of the variance, the second one (PC2) captures 4.93%, collectively representing 93.7% of the total variance. The highest contributor to both PCs is the phase between $1 \times 10^3$ and $1 \times 10^4$ Hz, followed by a much lower contribution of Zim for PC1 and Zre for PC2. We observe two clear clusters, overlapping around zero and diverging over both axes (corresponding with both color groups). Secondly, we note clustering between the different markers, representing the different electrode sizes.

PCA plots are effective ways to portray complex impedance datasets and are often used to facilitate the distinction between

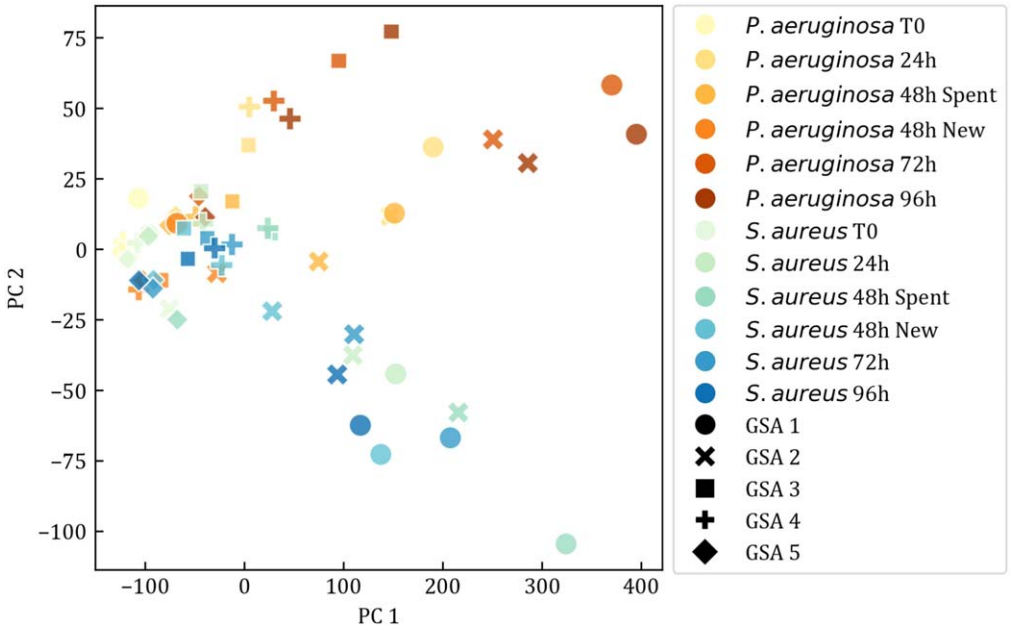


**Figure 9.** PCA plot produced considering median values over all frequencies of log normalized $|Z|$, Zim, Zre and Phase, representing all time points (T0, 24h, 48h Spent, 48h New, 72h and 96h) in yellow-red gradient for *P. aeruginosa* and in green-blue gradient for *S. aureus*, measured using the varying electrode sizes indicated by different markers.

different (biological) materials.[119] From this PCA, we can determine that there is some relation between the electrode size and the differentiation between bacteria and time points. Most notably, the largest differences can be seen for the largest electrodes (GSA 1, shown as dots in Fig. 9). As the electrode size becomes smaller, markers shift closer together and overlap, meaning they are increasingly similar in their impedimetric fingerprint. This culminates in GSA 5 (diamonds), for which all points are conglomerated around zero. This visual observation is confirmed when we determined the PCA scores per electrode group, where GSA 1 and 2 contribute the most to the variance. Additionally, we see a difference in the influence of electrode size between both bacteria. *P. aeruginosa* is clearly measurable over time using GSA 1, 2, 3 and 4. For *S. aureus*, only GSA 1 and 2 seem to capture the variance between time points.

Additionally, the markers for '48 h New' generally shift closer to zero for all electrode sizes. This change seems to be more pronounced for *P. aeruginosa*, indicating the importance of the metabolized medium for their detection. For *S. aureus*, even though only the larger electrodes can distinguish clearly between the time points, the '48 h New' shift toward zero is less severe. The importance of the phase around $4 \times 10^3$ Hz in the PCs indicates that the medium above the biofilm is actually the most important feature to detect the presence of bacteria and distinguish them, which further explains these shifts in '48 h New'.

This spatial distribution in the plot can be connected to earlier conclusions, as we observed larger changes in impedance for GSA 1 and 2. Secondly, the shift in impedance after medium renewal was also visible in Fig. 8. These observations spark interest as well as additional questions. As the phase around $4 \times 10^3$ Hz is the most important feature and there is a clear shift at 48 h New, it's important to consider that the medium's presence, containing metabolites that can be specific to certain species, contributes significantly to their characterization.

## Conclusions

In this work, we show not only that the interfacial impedance of pristine SIROF electrodes decreases significantly after potential cycling, but also that the selected scan rate has a strong impact on the final result. We can conclude that lower scan rates will result in a lower electrode impedance. However, for the fabricated SIROF electrodes in this work, the lowest impedance achievable was tied to extremely long pre-cycling times (i.e. a few days per electrode). Hence, a practical compromise was made, resulting in impedance values that were sufficiently low to enable biofilm detection. Furthermore, we demonstrated that SIROF electrodes could be effectively cleaned after usage for biofilm detection. The cleaning protocol resulted in sterile electrodes, and the resulting impedance after cleaning was comparable to the impedance before using the electrodes for biofilm detection.

Bacterial biofilms from *S. aureus* and *P. aeruginosa* can be detected and distinguished impedimetrically on SIROF microelectrodes. The electrodes are able to capture changes in biofilm growth over time, as well as distinguish between bacteria. Additionally, since the sensors' design included electrodes of different GSAs, we can give a recommendation for appropriate SIROF electrode sizes. According to our data, GSA 1 and 2 electrodes are the most efficient at capturing the biofilms growth as well as growth of planktonic bacteria and metabolites in the medium. They are, however, not usable for the differentiation between biofilms, which was only possible with GSA 3 through GSA 5. Since GSA 5 shows a less consistent relative change over time versus the other sizes, ideally the electrode should be in the GSA 3-4 range. We conclude that the ideal size for detection is not necessarily the same as characterization, since the GSA 1 electrodes capture differences over time on the surface and the bulk medium effectively, but were only able to detect differences between these species at 48 h. One can consider to include a range of electrodes with different geometrical surface areas on a single device, as a larger size may detect growth earlier, and a smaller size could then be used for fast characterization. Alternatively, to enable early biofilm detection and fast biofilm characterization for a fixed electrode area, one can consider to use slower pre-cycling scan speeds resulting in even lower electrode impedance, at the cost of an increased duration of the pre-cycling per electrode.

These conclusions provide a basis for the potential further development of this technology into miniaturized devices for implementation in situ or in vivo. For in situ applications, the sensor design could be amended to include a multi-well chamber. This would facilitate higher throughput measurements of bacterial

biofilms, which could then be implemented for the screening of novel antibiotics. The devices used for pre-cycling optimization feature a fabrication process that results in a long-term biocompatible and biostable electrode array, making them suitable for in vivo applications. While their potential for in vivo biofilm monitoring is promising, further in vivo experiments are required to validate their efficacy. Additionally, further research is needed to assess their capability for real-time, early biofilm detection and differentiation.

## Acknowledgments

This work was supported by FWO-Vlaanderen under grant FWO-SBO S007019N (Bisceps) and under grant SBO-FWO S000221N (Scatman). The authors would like to thank the following persons for useful discussions: Saeedeh Erbrahimi Takalloo from imec, Preston Donaldson, Maarten Cauwe, Lothar Mader, Esmaeil Afshari Savojbolagh from CMST, and Marco Francesco Carlino and Sergio Massaioli from ESAT/KUL. The authors would like to extend their gratitude to the support team of CMST for the extensive assistance with sample preparation to Karen Leus and Nathalie De Geyter (RUPT/UGent) for the XPS measurements, and to thank Dries Braeken for his contributions toward funding acquisition for this work.

## Author Contributions

**Grassi, Francesco**: Data curation (equal), Formal analysis (equal), Investigation (equal), Methodology (equal), Visualization (equal), Writing - Original draft preparation (equal), Writing - review and editing (equal). **Cums, Charlotte:** Data curation (equal), Formal analysis (equal), Investigation (equal), Methodology (equal) Project administration (Bisceps project), Visualization (equal), Writing - Original draft preparation (equal), Writing - review and editing (equal). **Cuypers, Dieter:** Investigation, Supervision. **Verplancke, Rik:** Investigation, Resources. **Vackier, Thijs:** Project administration (Bisceps project), Supervision, Writing - review and editing. **Schaubroeck, David:** Investigation. **Van Haeverbeke, Maxime:** Software. **Steenackers, Hans:** Funding acquisition (lead Bisceps project), Project administration (Bisceps project), Supervision, Writing - review and editing. **Op de Beeck, Maaike:** Funding acquisition (Bisceps and Scatman project), Project administration (Bisceps and Scatman project), Supervision, Writing - review and editing.

## Declaration of Interests

The authors declare that they have no known competing financial interests or personal relationships that could have appeared to influence the work reported in this paper.

## ORCID

Francesco Grassi https://orcid.org/0000-0003-4977-371X
Charlotte Cums https://orcid.org/0000-0002-6536-5508
Dieter Cuypers https://orcid.org/0000-0003-0550-6273
Rik Verplancke https://orcid.org/0000-0002-6642-9454
David Schaubroeck https://orcid.org/0000-0001-9576-3091
Maxime Van Haeverbeke https://orcid.org/0000-0001-7938-1675
Hans Steenackers https://orcid.org/0000-0001-5021-2069
Maaike Op de Beeck https://orcid.org/0000-0002-2700-6432

## References

1. M. Ghannoum, M. Parsek, M. Whiteley, and P. K. Mukherjee, *Microbial Biofilms* (John Wiley & Sons, Hoboken, New Jersey) (2020).
2. L. Karygianni, Z. Ren, H. Koo, and T. Thurnheer, "Biofilm matrixome: extracellular components in structured microbial communities." *Trends in Microbiology*, **28**, 668 (2020).
3. H.-C. Flemming, J. Wingender, U. Szewzyk, P. Steinberg, S. A. Rice, and S. Kjelleberg, "Biofilms: an emergent form of bacterial life." *Nature Reviews Microbiology*, **14**, 563 (2016).
4. J. Malviya et al., "Metabolomic profiling of bacterial biofilm: trends, challenges, and an emerging antibiofilm target." *World Journal of Microbiology and Biotechnology*, **39**, 212 (2023).
5. I. Guzmán-Soto, C. Mctiernan, M. Gonzalez-Gomez, A. Ross, K. Gupta, E. Suuronen, T.-F. Mah, M. Griffith, and E. Alarcon, "Mimicking biofilm formation and development: Recent progress in in vitro and in vivo biofilm models." *iScience*, **24**, 102443 (2021).
6. T.-F. Mah, "Biofilm-specific antibiotic resistance." *Future Microbiology*, **7**, 1061 (2012).
7. M. Cámara, W. Green, C. E. MacPhee, P. D. Rakowska, R. Raval, M. C. Richardson, J. Slater-Jefferies, K. Steventon, and J. S. Webb, "Economic significance of biofilms: a multidisciplinary and cross-sectoral challenge." *npj Biofilms and Microbiomes*, **8**, 1 (2022).
8. S. Mendhe, A. Badge, S. Ugemuge, and D. Chandi, "Impact of biofilms on chronic infections and medical challenges." *Cureus*, **15** (2023).
9. Z. Khatoon, C. D. McTiernan, E. J. Suuronen, T.-F. Mah, and E. I. Alarcon, "Bacterial biofilm formation on implantable devices and approaches to its treatment and prevention." *Heliyon*, **4** (2018).
10. G. Donelli, *Biofilm-based healthcare-associated infections: Volume I, vol. 831 of Advances in Experimental Medicine and Biology* (Springer, Cham Heidelberg New York Dordrecht London) (2014).
11. F. Lorenzo, M. Sanz-Puig, R. Bertó, and E. Orihuel, "Assessment of performance of two rapid methods for on-site control of microbial and biofilm contamination." *Applied Sciences*, **10**, 744 (2020).
12. M. Bassetti, M. Merelli, C. Temperoni, and A. Astilean, "New antibiotics for bad bugs: where are we?" *Annals of Clinical Microbiology and Antimicrobials*, **12**, 1 (2013).
13. A. Fernandes and M. Dias, "The microbiological profiles of infected prosthetic implants with an emphasis on the organisms which form biofilms." *Journal of Clinical and Diagnostic Research: JCDR*, **7**, 219 (2013).
14. M. Bassetti et al., "Systematic review of the impact of appropriate versus inappropriate initial antibiotic therapy on outcomes of patients with severe bacterial infections." *International Journal of Antimicrobial Agents*, **56**, 106184 (2020).
15. N. Silva, L. Marques, and D. Röder, "Diagnosis of biofilm infections: Current methods used, challenges and perspectives for the future." *Journal of Applied Microbiology*, **131**, 2148 (2021).
16. S. L. Percival, L. Suleman, C. Vuotto, and G. Donelli, "Healthcare-associated infections, medical devices and biofilms: risk, tolerance and control." *Journal of Medical Microbiology*, **64**, 323 (2015).
17. D. Neut, H. C. Van Der Mei, S. K. Bulstra, and H. J. Busscher, "The role of small-colony variants in failure to diagnose and treat biofilm infections in orthopedics." *Acta Orthopaedica*, **78**, 299 (2007).
18. L. Váradi, J. L. Luo, D. E. Hibbs, J. D. Perry, R. J. Anderson, S. Orenga, and P. W. Groundwater, "Methods for the detection and identification of pathogenic bacteria: past, present, and future." *Chem. Soc. Rev.*, **46**, 4818 (2017).
19. L. Polerecky, J. M. Klatt, M. Al-Najjar, and D. de Beer, "Hyper-spectral imaging of biofilm growth dynamics." *First Workshop on Hyperspectral Image and Signal Processing: Evolution in Remote Sensing*, Grenoble, France, 26-28 August 20091 (2009).
20. T. Mortier, A. D. Wieme, P. Vandamme, and W. Waegeman, "Bacterial species identification using maldi-tof mass spectrometry and machine learning techniques: A large-scale benchmarking study." *Computational and Structural Biotechnology Journal*, **19**, 6157 (2021).
21. P. Aguiar, R. Menezes, M. Penatti, T. Moreira, J. Pimenta, N. Silva, and D. Röder, "Rapid detection of biofilm-producing candida species via MALDI-TOF mass spectrometry." *J. Appl. Microbiol.*, **131**, 2049 (2021).
22. A. Gaudreau et al., "Evaluation of maldi-tof mass spectrometry for the identification of bacteria growing as biofilms." *J. Microbiol. Methods*, **145**, 79 (2018).
23. K. Zirk, M. Olze, and H. Pötzschke, "A simple method for the detection of biofilms using a heatable capacitive sensor structure (css): Description, proof of concept, and some technical improvements." *Sensors (Basel, Switzerland)*, **22**, 445 (2022).
24. R. Bhattacharya, K. Cornell, and J. Browning, "Simulation of a radio-frequency wave based bacterial biofilm detection method in dairy processing facilities." *Applied Sciences*, **14**, 4342 (2024).
25. S. Davis and M. R. Silva, "A proof-of-concept study on utilizing a novel non-invasive sensor for detection of thin biofilm in simulated water pipes." *Sensing and Imaging*, **22**, 1 (2021).
26. M. S. Mialich, J. F. Sicchieri, and A. J. Junior, "Analysis of body composition: a critical review of the use of bioelectrical impedance analysis." *Int. J. Clin. Nutr.*, **2**, 1 (2014).
27. J. B. van Duuren, M. Müsken, B. Karge, J. Tomasch, C. Wittmann, S. Häussler, and M. Brönstrup, "Use of single-frequency impedance spectroscopy to characterize the growth dynamics of biofilm formation in pseudomonas aeruginosa." *Sci. Rep.*, **7**, 1 (2017).
28. I. Tubia, J. Paredes, , and S. Arana, "Brettanomyces bruxellensis growth detection using interdigitated microelectrode based sensors by means of impedance analysis." *Sensors and Actuators A: Physical*, **269**, 175 (2018).
29. A. Turolla, M. Di Mauro, L. Mezzera, M. Antonelli, and M. Carminati, "Development of a miniaturized and selective impedance sensor for real-time slime monitoring in pipes and tanks." *Sensors and Actuators B: Chemical*, **281**, 288 (2019).
30. R. C. Huiszoon, S. Subramanian, P. Ramiah Rajasekaran, L. A. Beardslee, W. E. Bentley, and R. Ghodssi, "Flexible Platform for In Situ Impedimetric Detection and Bioelectric Effect Treatment of Escherichia Coli Biofilms." *IEEE Transactions on Biomedical Engineering*, **66**, 1337 (2019).

31. P. P. Sedghizadeh et al., "Real-time impedance-based monitoring of the growth and inhibition of osteomyelitis biofilm pathogen staphylococcus aureus treated with novel bisphosphonate-fluoroquinolone antimicrobial conjugates." *International Journal of Molecular Sciences*, **24**, 1985 (2023).
32. S. Kumar, A. T. Nguyen, S. Goswami, J. Ferracane, and D. Koley, "Real-time monitoring of local pH and biofilm formation using a noninvasive impedance-based method." *SSRN Electronic Journal*, **376**(A), 133034 (2022).
33. S. Kumar, A. T. Nguyen, S. Goswami, J. Ferracane, and D. Koley, "Real-time monitoring of biofilm formation using a noninvasive impedance-based method." *Sensors and Actuators B: Chemical*, **376**, 133034 (2023).
34. E. Goikoetxea, D. Routkevitch, A. de Weerdt, J. J. Green, H. Steenackers, and D. Braeken, "Impedimetric fingerprinting and structural analysis of isogenic e. coli biofilms using multielectrode arrays." *Sensors and Actuators, B: Chemical*, **263**, 319 (2018).
35. M. Van Haeverbeke, C. Cums, T. Vackier, D. Braeken, M. Stock, H. Steenackers, and B. De Baets, "Impedimetric biofilm characterization with microelectrode arrays using equivalent electrical circuit features and ensemble classifiers." *Chemometrics and Intelligent Laboratory Systems*, **244**, 105048 (2024).
36. M. Janders, U. Egert, M. Stelzle, and W. Nisch, "Novel thin film titanium nitride micro-electrodes with excellent charge transfer capability for cell stimulation and sensing applications." *Proceedings of 18th Annual International Conference of the IEEE Engineering in Medicine and Biology Society*, Amsterdam, Netherlands, 31 October 1996 - 03 November 1996 (IEEE) **1**, 245 (1996).
37. G. Sánchez, E. Dalchiele, and A. Bologna Alles, "Electrical characterization of titanium nitride surfaces for pacing electrodes." *Journal of Materials Science*, **41**, 3241 (2006).
38. H. Jang and J. Lee, "Iridium oxide fabrication and application: a review." *Journal of Energy Chemistry*, **46**, 152 (2020).
39. T. Katsube, I. Lauks, and J. Zemel, "pH-sensitive sputtered iridium oxide films." *Sens. Actuators*, **2**, 399 (1981).
40. S. F. Cogan, T. D. Plante, and J. Ehrlich, "Sputtered indium oxide films (SIROFs) for low-impedance neural stimulation and recording electrodes." *The 26th Annual International Conference of the IEEE Engineering in Medicine and Biology*, San Francisco, CA, USA01-05 September 2004 (IEEE) **26**, 4153 (2004).
41. P. Steegstra, "Hydrous Iridium Oxide for In-Situ pH Sensing: Electrodeposition, Properties and Applications." *PhD Thesis*, University of Gothenburg. Faculty of Science (2013) 9789162884796.
42. S. Bause, M. Decker, F. Gerlach, J. Näther, F. Köster, P. Neubauer, and W. Vonau, "Development of an iridium-based pH sensor for bioanalytical applications." *Journal of Solid State Electrochemistry*, **22**, 51 (2018).
43. X. Guimerà, A. Moya, A. D. Dorado, X. Illa, R. Villa, D. Gabriel, X. Gamisans, and G. Gabriel, "A minimally invasive microsensor specially designed for simultaneous dissolved oxygen and pH biofilm profiling." *Sensors*, **19**, 4747 (2019).
44. P. VanHoudt, Z. Lewandowski, and B. Little, "Iridium oxide pH microelectrode." *Biotechnology and Bioengineering*, **40**, 601 (1992).
45. S. C. Dexter and P. Chandrasekaran, "Direct measurement of pH within marine biofilms on passive metals." *Biofouling*, **15**, 313 (2000).
46. J. Weiland and D. Anderson, "Chronic neural stimulation with thin-film, iridium oxide electrodes." *IEEE Transactions on Bio-Medical Engineering*, **47**, 911 (2000).
47. H. Singh, N. Sawal, V. K. Gupta, R. Jha, M. Stamm, S. Arjun, V. Gupta, and J. D. Rolston, "Increased electrode impedance as an indicator for early detection of deep brain stimulation (dbs) hardware infection: Clinical experience and in vitro study." *Journal of Clinical Neuroscience*, **120**, 76 (2024).
48. L. S. Robblee, J. L. Lefko, and S. B. Brummer, "Activated Ir: An electrode suitable for reversible charge injection in saline solution." *J. Electrochem. Soc.*, **130**, 731 (1983).
49. D. N. Buckley and L. D. Burke, "The oxygen electrode. Part 5.—Enhancement of charge capacity of an iridium surface in the anodic region." *J. Chem. Soc.,Faraday Trans. 1 F*, **71**, 1447 (1975).
50. J. O. Zerbino, N. R. De Tacconi, and A. J. Arvìa, "The activation and deactivation of iridium electrodes in acid electrolytes." *J. Electrochem. Soc.*, **125**, 1266 (1978).
51. B. Wessling, A. Besmehn, W. Mokwa, and U. Schnakenberg, "Reactively sputtered iridium oxide: influence of plasma excitation and substrate temperature on morphology, composition, and electrochemical characteristics." *J. Electrochem. Soc.*, **154**, F83 (2007).
52. X. Kang, J. Liu, H. Tian, B. Yang, Y. Nuli, and C. Yang, "Optimization and electrochemical characterization of RF-sputtered iridium oxide microelectrodes for electrical stimulation." *J. Micromech. Microeng.*, **24**, 025015 (2014).
53. S. Negi, R. Bhandari, L. Rieth, and F. Solzbacher, "Effect of sputtering pressure on pulsed-DC sputtered iridium oxide films." *Sens. Actuators, B*, **137**, 370 (2009).
54. A. Van Ooyen, G. Topalov, G. Ganske, W. Mokwa, and U. Schnakenberg, "Iridium oxide deposited by pulsed dc-sputtering for stimulation electrodes." *J. Micromech. Microeng.*, **19**, 074009 (2009).
55. S. F. Cogan, J. Ehrlich, T. D. Plante, A. Smirnov, D. B. Shire, M. Gingerich, and J. F. Rizzo, "Sputtered iridium oxide films for neural stimulation electrodes." *J. Biomed. Mater. Res. Part B*, **89**, 353 (2009).
56. S. Gawad, M. Giugliano, M. Heuschkel, B. Wessling, H. Markram, U. Schnakenberg, P. Renaud, and H. Morgan, "Substrate arrays of iridium oxide microelectrodes for in vitro neuronal interfacing." *Front. Neuroeng.*, **2** (2009).
57. B. Wessling, W. Mokwa, and U. Schnakenberg, "Sputtered Ir films evaluated for electrochemical performance I. Experimental results." *J. Electrochem. Soc.*, **155**, F61 (2008).
58. E. Slavcheva, U. Schnakenberg, and W. Mokwa, "Deposition of sputtered iridium oxide-Influence of oxygen flow in the reactor on the film properties." *Appl. Surf. Sci.*, **253**, 1964 (2006).
59. T. Boretius and T. Stieglitz, "The influence of hot-steam sterilization on hydrated sputtered iridium oxide films." *6th International IEEE/EMBS Conference on Neural Engineering (NER)*, San Diego, CA, USA 06-08 November 2013 (IEEE) **2013**, 279 (2013).
60. J. Newman, "Resistance for flow of current to a disk." *J. Electrochem. Soc.*, **113**, 501 (1966).
61. D. A. Stenger and T. M. McKenna, "Microelectrode Models for Neural Interfaces." *Enabling Technologies for Cultured Neural Networks* (Academic Press, San Diego, CA)7, 355 (1994) 0126659702.
62. M. Op de Beeck et al., "Ultra-thin biocompatible implantable chip for bidirectional communication with peripheral nerves." *2017 IEEE Biomedical Circuits and Systems Conference (BioCAS)*, Turin, Italy, 19-21 October 2017 (IEEE) (2018).
63. S. F. Cogan, "Neural stimulation and recording electrodes." *Annual Review of Biomedical Engineering*, **10**, 275 (2008).
64. M. F. Yuen, I. Lauks, and W. C. Dautremont-Smith, "pH dependent voltammetry of iridium oxide films." *Solid State Ionics*, **11**, 19 (1983).
65. E. Slavcheva, R. Vitushinsky, W. Mokwa, and U. Schnakenberg, "Sputtered iridium oxide films as charge injection material for functional electrostimulation." *J. Electrochem. Soc.*, **151**, E226 (2004).
66. C. Boehler, S. Carli, L. Fadiga, T. Stieglitz, and M. Asplund, "Tutorial: Guidelines for standardized performance tests for electrodes intended for neural interfaces and bioelectronics." *Nature Protocols*, **15**, 3557 (2020).
67. R. S. Musa, "Design, Fabrication, and Characterization of a Neural Probe for Deep Brain Stimulation and Recording." *PhD thesis*, KU Leuven (2011), https://lirias.kuleuven.be/retrieve/159421.
68. S. Fleischmann, J. B. Mitchell, R. Wang, C. Zhan, D.-e. Jiang, V. Presser, and V. Augustyn, "Pseudocapacitance: From Fundamental Understanding to High Power Energy Storage Materials." *Chem. Rev.*, **120**, 6738 (2020).
69. J.-C. Lassegues and D. Rodriguez, "Smart window using a proton-conducting polymer as electrolyte." *Optical Materials Technology for Energy Efficiency and Solar Energy Conversion XI: Chromogenics for Smart Windows, SPIE*, **1728**, 241 (1992).
70. J. Klein, S. Clauson, and S. Cogan, "Reactive IrO 2 sputtering in reducing/oxidizing atmospheres." *J. Mater. Res.*, **10**, 328 (1995).
71. J. Maeng, B. Chakraborty, N. Geramifard, T. Kang, R. T. Rihani, A. Joshi-Imre, and S. F. Cogan, "High-charge-capacity sputtered iridium oxide neural stimulation electrodes deposited using water vapor as a reactive plasma constituent." *Journal of Biomedical Materials Research Part B: Applied Biomaterials*, **108**, 880 (2020).
72. N. Geramifard, B. Chakraborty, B. Dousti, G. S. Lee, and J. Maeng, "High-Energy-Density Sputtered Iridium Oxide Micro-Supercapacitors Operating in Physiological Electrolytes." *J. Electrochem. Soc.*, **169**, 050508 (2022).
73. J. D. Klein, S. L. Clauson, and S. F. Cogan, "Morphology and charge capacity of sputtered iridium oxide films." *Journal of Vacuum Science & Technology A: Vacuum, Surfaces, and Films*, **7**, 3043 (1989).
74. D. M. Mattox, "The "good" vacuum (low pressure) processing environment." *Handbook of Physical Vapor Deposition (PVD) Processing*, ed. D. M. Mattox (William Andrew Publishing, Boston) 2nd ed ed., 3, 73–145 (2010).
75. L. Yang, C. Ruan, and Y. Li, "Detection of viable salmonella typhimurium by impedance measurement of electrode capacitance and medium resistance." *Biosensors and Bioelectronics*, **19**, 495 (2003).
76. R. Gomez-Sjoberg, D. Morisette, and R. Bashir, "Impedance microbiology-on-a-chip: microfluidic bioprocessor for rapid detection of bacterial metabolism." *Journal of Microelectromechanical Systems*, **14**, 829 (2005).
77. A. Zikmund, P. Ripka, L. Krasny, T. Judl, and D. Jahoda, "Biofilm detection by the impedance method." *3rd International Conference on Biomedical Engineering and Informatics*, Yantai, China, 16-18 October 2010 (IEEE) **4**, 1432 (2010).
78. X. Muñoz-Berbel, R. Escudé-Pujol, N. Vigués, M. Cortina-Puig, C. Garcìa-Aljaro, J. Mas, and F. X. Muñoz, "Real time automatic system for the impedimetric monitoring of bacterial growth." *Analytical Letters*, **44**, 2571 (2011).
79. K. Settu, C.-J. Chen, J.-T. Liu, C.-L. Chen, and J.-Z. Tsai, "Impedimetric method for measuring ultra-low E. coli concentrations in human urine." *Biosensors and Bioelectronics*, **66**, 244 (2015).
80. R. Sheybani and A. Shukla, "Highly sensitive label-free dual sensor array for rapid detection of wound bacteria." *Biosensors and Bioelectronics*, **92**, 425 (2017).
81. M. Méndez-Tovar, J. V. Garcìa-Meza, and I. González, "Electrochemical monitoring of Acidithiobacillus thiooxidans biofilm formation on graphite surface with elemental sulfur." *Bioelectrochemistry*, **128**, 30 (2019).
82. S. E. Astorga, L. X. Hu, E. Marsili, and Y. Huang, "Electrochemical signature of escherichia coli on nickel micropillar array electrode for early biofilm characterization." *ChemElectroChem*, **6**, 4674 (2019).
83. S. E. Astorga, L. X. Hu, E. Marsili, and Y. Huang, "Ordered micropillar array gold electrode increases electrochemical signature of early biofilm attachment." *Materials & Design*, **185**, 108256 (2020).
84. J. Song, Y. Li, F. Yin, Z. Zhang, D. Ke, D. Wang, Q. Yuan, and X.-E. Zhang, "Enhanced electrochemical impedance spectroscopy analysis of microbial biofilms on an electrochemically In Situ generated graphene interface." *ACS Sensors*, **5**, 1795 (2020), Publisher: American Chemical Society.
85. M. Wolf-Baca, T. Grzebyk, and A. Siedlecka, "Detection of biofilm on water supply technical materials with the application of an impedance sensor." *International Journal of Environmental Research*, **16**, 64 (2022).
86. M. Moradi, G. Ghiara, R. Spotorno, D. Xu, and P. Cristiani, "Understanding biofilm impact on electrochemical impedance spectroscopy analyses in microbial corrosion and microbial corrosion inhibition phenomena." *Electrochimica Acta*, **426**, 140803 (2022).
87. S. Liang, M. Hu, B. Li, D. Xia, C. Liang, F. Peng, and D. Wang, "Smart implant with bacteria monitoring and killing ability for orthopedic applications." *ACS Applied Materials & Interfaces*, **15**, 29889 (2023).

88. J. Fojt, E. Průchová, and V. Hybášek, "Electrochemical impedance response of the nanostructured Ti-6Al-4V surface in the presence of S. aureus and E. coli." *Journal of Applied Electrochemistry*, **53**, 2153 (2023).
89. M. Varshney and Y. Li, "Double interdigitated array microelectrode-based impedance biosensor for detection of viable Escherichia coli O157:H7 in growth medium." *Talanta*, **74**, 518 (2008).
90. J. J. Goncalves and R. Govind, "Rapid evaluation of biofilm attachment promoters and biofilm growth orientation using a mini-impedimetric device." *Sensors and Actuators B: Chemical*, **143**, 341 (2009).
91. J. Paredes, S. Becerro, F. Arizti, A. Aguinaga, J. L. Del Pozo, and S. Arana, "Real time monitoring of the impedance characteristics of Staphylococcal bacterial biofilm cultures with a modified CDC reactor system." *Biosensors and Bioelectronics*, **38**, 226 (2012).
92. J. Paredes, S. Becerro, and S. Arana, "Label-free interdigitated microelectrode based biosensors for bacterial biofilm growth monitoring using Petri dishes." *Journal of Microbiological Methods*, **100**, 77 (2014).
93. J. Paredes et al., "Smart central venous port for early detection of bacterial biofilm related infections." *Biomedical Microdevices*, **16**, 365 (2014).
94. M. C. Bonetto, N. J. Sacco, A. H. Ohlsson, E. Cortón, D. Sticker, V. Charwat, and P. Ertl, "Rapid and label-free differentiation of bacterial strains using low frequency electrochemical impedance spectroscopy." *2014 IEEE 9th IberoAmerican Congress on Sensors*, Bogota, Colombia, 15-18 October 2014, 1 (2014).
95. K. Chabowski, A. F. Junka, P. Szymczyk, T. Piasecki, A. Sierakowski, B. Maczynska, and K. Nitsch, "The application of impedance microsensors for real-time analysis of Pseudomonas aeruginosa biofilm formation." *Polish Journal of Microbiology*, **64**, 115 (2015).
96. S. Subramanian, R. Huiszoon, W. E. Bentley, and R. Ghodssi, "Micro FBI: A microsystem for feedback-based biofilm inhibition." *2016 IEEE Sensors*, Orlando, FL, USA30 October 2016 - 03 November 2016 (IEEE) 1 (2016).
97. S. Brosel-Oliu, O. Mergel, N. Uria, N. Abramova, P. Van Rijn, and A. Bratov, "3D impedimetric sensors as a tool for monitoring bacterial response to antibiotics." *Lab Chip*, **19**, 1436 (2019).
98. J. E. Aranzazu-Osorio and L. H. Alzate, "Evaluation of Pseudomonas sp. growth in culture medium using electrical impedance spectroscopy with two bipolar geometries." *J. Phys.: Conf. Ser.*, *3rd Latin-American Conference on Bioimpedance*, Manizales, Colombia, South America, 3-5 oktober 2018 J. Phys.: Conf. Ser.,1272, 012014 (2019).
99. G. Gula, P. Szymanowska, T. Piasecki, S. Góras, T. Gotszalk, and Z. Drulis-Kawa, "The application of impedance spectroscopy for Pseudomonas biofilm monitoring during phage infection." *Viruses*, **12**, 407 (2020).
100. M. C. Romero, G. Ramos, I. González, and F. Ramìrez, "A novel method to reveal a ureolytic biofilm attachment and in situ growth monitoring by electrochemical impedance spectroscopy." *Applied Biochemistry and Biotechnology*, **193**, 1379 (2021).
101. A. J. Hannah, A. C. Ward, and P. Connolly, "Rapidly detected common wound pathogens via easy-to-use electrochemical sensors." *Journal of Biomedical Engineering and Biosciences*, **8**, 11 (2021).
102. J. Song, Y. Li, D. Ke, D. Wang, and X.-E. Zhang, "In situ graphene-modified carbon microelectrode array biosensor for biofilm impedance analysis." *Electrochimica Acta*, **403**, 139570 (2022).
103. S. Werwinski, J. A. Wharton, M. Nie, and K. R. Stokes, "Monitoring aerobic marine bacterial biofilms on gold electrode surfaces and the influence of nitric oxide attachment control." *Anal. Chem.*, **94**, 12323 (2022), Publisher: American Chemical Society.
104. M. McGlennen, M. Dieser, C. M. Foreman, and S. Warnat, "Using Electrochemical Impedance Spectroscopy to Study Biofilm Growth in a 3d-Printed Flow Cell System." *Biosensors and Bioelectronics: X*, **14**, 100326 (2023).
105. D. Sridharan, C. Karthikeyan, S. Maruthamuthu, and N. Palaniswamy, "Electrochemical investigation of freshwater biofilm on FTO surface: Oxide film perspective." *ChemistrySelect*, **7** (2022).
106. J. Pellé, M. Longo, N. Le Poul, C. Hellio, S. Rioual, and B. Lescop, "Electrochemical monitoring of the Pseudomonas aeruginosa growth and the formation of a biofilm in TSB media." *Bioelectrochemistry*, **150**, 108344 (2023).
107. M. Varshney and Y. Li, "Interdigitated array microelectrodes based impedance biosensors for detection of bacterial cells." *Biosensors and Bioelectronics*, **24**, 2951 (2009).
108. A. C. Ward, P. Connolly, and N. P. Tucker, "Pseudomonas aeruginosa can be detected in a polymicrobial competition model using impedance spectroscopy with a novel biosensor." *PLOS One*, **9**, e91732 (2014).
109. A. Ghanbari, J. Dehghany, T. Schwebs, M. Müsken, S. Häussler, and M. Meyer-Hermann, "Inoculation density and nutrient level determine the formation of mushroom-shaped structures in pseudomonas aeruginosa biofilms." *Sci. Rep.*, **6**, 1 (2016).
110. A. Atabek and T. A. Camesano, "Atomic force microscopy study of the effect of lipopolysaccharides and extracellular polymers on adhesion of Pseudomonas aeruginosa." *Journal of Bacteriology*, **189**, 8503 (2007).
111. J. L. Connell, J. Kim, J. B. Shear, A. J. Bard, and M. Whiteley, "Real-time monitoring of quorum sensing in 3d-printed bacterial aggregates using scanning electrochemical microscopy." *Proceedings of the National Academy of Sciences*, **111**, 18255 (2014).
112. O. Simoska, M. Sans, M. D. Fitzpatrick, C. M. Crittenden, L. S. Eberlin, J. B. Shear, and K. J. Stevenson, "Real-time electrochemical detection of pseudomonas aeruginosa phenazine metabolites using transparent carbon ultramicroelectrode arrays." *ACS Sens.*, **4**, 170 (2018).
113. D. Koley, M. M. Ramsey, A. J. Bard, and M. Whiteley, "Discovery of a biofilm electrocline using real-time 3d metabolite analysis." *Proceedings of the National Academy of Sciences*, **108**, 19996 (2011).
114. D. L. Bellin, H. Sakhtah, J. K. Rosenstein, P. M. Levine, J. Thimot, K. Emmett, L. E. Dietrich, and K. L. Shepard, "Integrated circuit-based electrochemical sensor for spatially resolved detection of redox-active metabolites in biofilms." *Nat. Commun.*, **5**, 3256 (2014).
115. D. L. Bellin, H. Sakhtah, Y. Zhang, A. Price-Whelan, L. E. Dietrich, and K. L. Shepard, "Electrochemical camera chip for simultaneous imaging of multiple metabolites in biofilms." *Nat. Commun.*, **7**, 10535 (2016).
116. J. Elliott, O. Simoska, S. Karasik, J. B. Shear, and K. J. Stevenson, "Transparent carbon ultramicroelectrode arrays for the electrochemical detection of a bacterial warfare toxin, pyocyanin." *Anal. Chem.*, **89**, 6285 (2017).
117. J. Jia, S.-R. Kwon, S. Baek, V. Sundaresan, T. Cao, A. R. Cutri, K. Fu, B. Roberts, J. D. Shrout, and P. W. Bohn, "Actively controllable solid-phase microextraction in a hierarchically organized block copolymer-nanopore electrode array sensor for charge-selective detection of bacterial metabolites." *Anal. Chem.*, **93**, 14481 (2021).
118. H. Do, S.-R. Kwon, S. Baek, C. S. Madukoma, M. K. Smiley, L. E. Dietrich, J. D. Shrout, and P. W. Bohn, "Redox cycling-based detection of phenazine metabolites secreted from pseudomonas aeruginosa in nanopore electrode arrays." *Analyst*, **146**, 1346 (2021).
119. W. S. R. Teixeira, M. K. L. Silva, D. Grasseschi, C. A. Senna, A. G. de Oliveira, J. Gruber, I. Cesarino, and M. O. Salles, "Principal component analysis as a tool for electrochemical characterization of modified electrodes: a case study." *J. Electrochem. Soc.*, **169**, 047526 (2022).